Laminar jets of Bingham-plastic liquids

K. R. J. Ellwood,[a] G. C. Georgiou, T. C. Papanastasiou, and J. O. Wilkes

Department of Chemical Engineering, The University of Michigan, Ann Arbor, Michigan 48109

(Received 30 October 1989; accepted 28 February 1990)

Synopsis

The steady and transient behavior of jets generated by circular and slit nozzles are analyzed by the Galerkin finite-element method with free-surface parametrization and Newton iteration. A novel constitutive equation is used to approximate Bingham liquids that is valid uniformly in yielded and unyielded domains and which approximates the ideal Bingham model and the Newtonian liquid in its two limiting behaviors. At steady state the influence of yield stress on the die swell is equivalent to that of surface tension; that is, suppression of jet diameter at low Reynolds numbers and necking at high Reynolds number. The predictions at high Reynolds numbers agree with the asymptotic behavior at infinite Reynolds number of the jet far downstream. In the transient analysis, surface tension destabilizes round jets and increases the size of satellite drops. Yield stress was found to retard jet breakup times in addition to producing smaller satellites. Shear thinning was found to result in shorter collapse times than those for Newtonian fluid; furthermore, the satellite drop size increased with increasing shear thinning. The nonlinear analysis predicts that, although round jet breakup may occur spontaneously by surface tension, an external factor, commonly air shear, must be applied to break a planar jet at Reynolds numbers below its transition to a turbulent jet.

I. INTRODUCTION

A class of materials exhibit little or no deformation up to a certain level of stress, called the yield stress. These materials are often called Bingham plastics, after Bingham,[1] who first described paint in this way in 1919, and were first analyzed by Oldroyd,[2] Reiner,[3] and Prager.[4] Paint, slurries, pastes, and food substances like margarine, mayonnaise,

[a]To whom correspondence should be addressed.

and ketchup are good examples of Bingham plastics. A list of several materials exhibiting yield was given recently by Bird *et al.*[5] Production of composite materials usually involves processing of fiber suspensions that often exhibit yield behavior.[6] Concentrated suspensions of solid particles in Newtonian liquids show a yield stress followed by nearly Newtonian behavior after yielding and flow.

To model the stress-deformation behavior, several constitutive relations have been proposed,[7,8] and different yield criteria have been used.[9] The state of affairs is empirical and relatively undeveloped, partially due to the difficulty of obtaining accurate, reliable data on these materials at vanishingly small deformation, which is necessary to determine the existence and the level of the yield stress. The most common three-dimensional constitutive relation uses the von Mises criterion which predicts that the material flows and deforms significantly only when the second invariant of the stress tensor exceed the yield stress; otherwise the material behaves like a strained solid.

Figure 1 shows this behavior of stress as a function of the rate of strain for a shear flow. The existence of a true yield stress, and therefore the accuracy of the von Mises criterion, has been questioned by several investigators. In a recent paper,[10] Barnes and Walters concluded that *no yield stress exists* given accurate measurements, however this was disputed recently by Hartnett and Hu.[11] Given these "engineering realities",[12] the material can be well approximated uniformly at all levels of stress as a liquid that exhibits infinitely high viscosity in the limit of low shear rates followed by a continuous transition to a viscous liquid. The approximation can be made more and more accurate at even vanishingly small shear rates by means of a material parameter that controls the exponential growth of stress, according to the following constitutive equation proposed by Papanastasiou[13] and shown in Fig. 1:

$$\tau = 2\left\{\mu + \frac{\tau_y}{|2\Pi_{\mathbf{D}}|^{1/2}}[1 - \exp(-m|\Pi_{\mathbf{D}}|^{1/2})]\right\}\mathbf{D}. \tag{1}$$

Here τ_y is the apparent yield stress and m is a stress growth exponent. $\mathbf{D}$ is the rate of strain tensor, and $\Pi_{\mathbf{D}}$ its second invariant. Equation (1) approximates the von Mises criterion for relatively big exponent m, and holds uniformly in yielded and unyielded regions. Actually, extensive experimental results,[14–16] including ours with solvent-based paints (Fig. 1) show that, in most instances, Eq. (1) provides a better approximation to real data than the ideal Bingham plastic model as shown in Fig. 1. The data of Fig. 1 were taken by means of a Brookfield viscometer equipped with a relaxation mechanism to measure stress down to shear

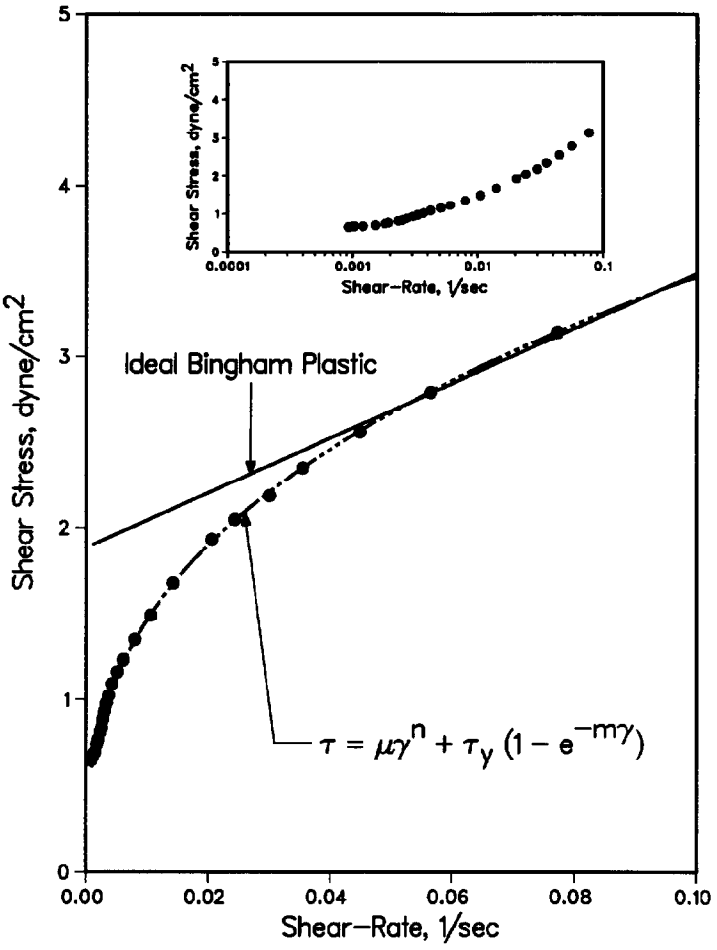

FIG. 1. Experimental data for a sample water-borne paint demonstrating the applicability of Eq. (1) to Bingham-plastic liquids. (● is a white basecoat—Dupont 408-6-80179.)

rates of the order of 10^{-3} s^{-1}, where the yield stress becomes important. Thus Eq. (1) is exact for these nearly ideal Bingham liquids and approximates well the ideal Bingham liquid—which may be only a theoretical idealization since rheological measurements with existing rheometers are incapable of conducting measurements at vanishingly small deformations where the yield stress is detected. In the limit of

$m \to \infty$, the predictions of Eq. (1) become virtually independent of m at finite values of $m > 50$ which practically may be taken to correspond to the ideal Bingham liquid, as will be demonstrated in the discussion of the results.

From the computational point of view, Eq. (1) is by far superior to the von Mises criterion because it holds uniformly in both yielded and unyielded regions and so the necessity to track yield surfaces or lines is eliminated which significantly simplifies computations in complex geometries. Computational methods for Bingham liquids track yield lines which separate regions of the two states[17] or else rely on biviscosity discontinuous representations.[18–20] Two recent methods[14,21] avoided the tracking of yield surfaces by employing constitutive equations that hold everywhere continuously by replacing the mathematical interface between yielded and unyielded regions with a sigmoidal transition of viscosity which can be made steeper by increasing the exponent m as shown by Fig. 1. Thus, it appears that Eq. (1) is appropriate for Bingham plastics both, with respect to physical significance and, primarily, computational efficiency. The material parameters τ_y and m can easily be fitted from data as suggested by Fig. 1.

Numerous fundamental yet pioneering studies concerning jet stability are present in the literature with the earliest being that of Lord Rayleigh.[22] Rayleigh examined the breakup of an inviscid axisymmetric liquid jet using linear stability theory in which the growth of infinitesimal periodic disturbances is determined. Chandrasekhar later extended the results of Rayleigh and provided a full account of the contributions of large viscosity and magnetic stress to jet breakup.[23]

The stability analysis of non-Newtonian jets,[24] particularly Bingham-plastic jets is still relatively undeveloped. Among the earliest to consider a completely nonlinear jet stability analysis were Keunings[25] and Bousfield *et al.*[26] where the stabilizing influence of viscoelasticity was investigated. This was in good agreement with experimental observations and demonstrated the inadequacy of linear theory which, in their case, gave contradictory results. The only experimental investigation concerning fluids with yield stress was conducted by Goldin *et al.*[27] in which a linear theory, based on a constant bulk average viscosity, was used to predict jet breakup lengths. In this work, steady finite jets emerging from slit and round orifices and infinite transient jets are examined by means of a two-dimensional, steady and transient analysis, respectively, for Newtonian, viscous shear thinning, and Bingham-plastic liquids approximated by Eq. (1). This analysis is important in understanding a

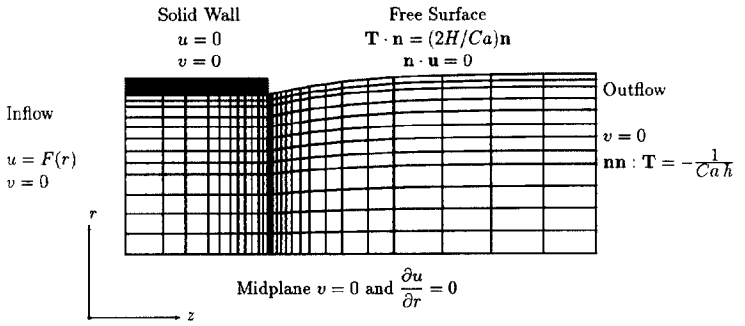

FIG. 2. Domain, governing equations, and boundary conditions for the round jet.

number of processes such as coating or painting by atomization, ink-jet printing, and the development of antimisting agents for flammable materials.

II. FORMULATION

The flow configuration and coordinates for the steady axisymmetric jet are defined in Fig. 2 (a similar configuration exists for the planar jet). The flow is steady and incompressible and is governed by the momentum and continuity equations along with the boundary conditions. The inflow and outflow boundaries are taken at finite distances L_1 and L_2, sufficiently far from the exit so that the flow can be considered fully developed at the inlet, and uniform at the outflow plane. Thus the boundary conditions at the outlet are

$$\mathbf{T}:\mathbf{nn} = -\frac{1}{\mathrm{Ca}\,h_f}, \quad v=0, \tag{2}$$

where $\mathbf{T}$ is the dimensionless total stress tensor, $\mathbf{n}$ the normal to outflow plane, v the radial velocity, $\mathrm{Ca} \equiv \mu U/\sigma$ the capillary number, and h_f the dimensionless final jet radius. The scales used for the length, velocity, and stress are R, U, and $\mu U/R$, where R is the radius of the pipe or the half-width of the slit and U is the average fluid velocity.

The analytic solution of slit or pipe flow is used as the essential condition at the inlet. The dimensionless inlet velocity for these flows is given by

$$u = \tfrac{1}{2}C(1 - r^2) - T_y(1 - r), \quad H \leqslant r \leqslant 1 \tag{3}$$

and

$$u=\tfrac{1}{2}C(1-H^2)-T_y(1-H), \quad 0\leqslant r\leqslant H, \tag{4}$$

respectively, where

$$H=T_y/C, \tag{5}$$

is the distance of the yield surface from the midplane at the inlet and $C=\Delta P/\Delta L$ is the dimensionless constant pressure gradient of a fully developed flow at the inlet corresponding to a defined flow rate and $T_y=\tau_y R/\mu U$ is the dimensionless yield stress. It transpires for the slit, that

$$C=(2+T_y)\left(\frac{1}{2}+\cos\left\{\frac{1}{3}\cos^{-1}\left[1-\frac{2T_y^3}{(2+T_y)^3}\right]\right\}\right). \tag{6}$$

For the pipe, C is the largest root of

$$3C^4-4(3+T_y)C^3+T_y^4=0. \tag{7}$$

In the finite-element formulation the unknown velocities, pressures, and jet profile ($\mathbf{u}$, p, and h) are expanded in terms of biquadratic Φ^i, bilinear ψ^i, and quadratic $\Phi^i|_{\eta=1}$, basis functions, respectively:

$$\mathbf{u}=\sum_{i=1}^{N}\mathbf{u}_i\Phi^i(\xi,\eta), \quad p=\sum_{i=1}^{M}p_i\Psi^i(\xi,\eta), \quad h=\sum_{i=1}^{S}h_i\Phi^i(\xi,\eta=1), \tag{8}$$

where ξ and η are the isoparametric coordinates. The Galerkin residuals are calculated by weighting the continuity, momentum, and kinematic equations with Ψ^i, Φ^i, and $\Phi^i|_{\eta=1}$, respectively:

$$R_C^i=\int_V \nabla\cdot\mathbf{u}\Psi^i\,dV=0, \quad i=1,2,\ldots,M, \tag{9}$$

$$\mathbf{R}_M^i=\int_V [\nabla\cdot\mathbf{T}-\mathrm{Re}\,\mathbf{u}\cdot\nabla\mathbf{u}]\Phi^i\,dV=0, \quad i=1,2,\ldots,N, \tag{10}$$

$$R_K^i=\int_{S_3}\mathbf{n}\cdot\mathbf{u}\Phi^i|_{\eta=1}\,dV=0, \quad i=1,2,\ldots,S. \tag{11}$$

Here $\mathrm{Re}=2\rho UR/\mu$ is the Reynolds number. The Galerkin procedure, including the projection of the three-dimensional domain onto a tessellation of an r–z plane, and the isoparametric mapping to the rectilinear computational domain, can be found elsewhere.[28] The final forms of the weighted equations on the computational isoparametric domain are

$$R_C^i = -\int_{-L_1}^{L_2}\int_0^h \left[\left(\frac{\partial u}{\partial z}+\frac{\partial v}{\partial r}\right)r^\alpha + \alpha v\right]\Psi^i |J|\, d\xi\, d\eta,$$
$$i=1,2,\ldots,M, \tag{12}$$

$$R_u^i = -\int_{L_1}^{L_2}\int_0^h \left[T^{zz}\frac{\partial \Phi^i}{\partial z} + T^{zr}\frac{\partial \Phi^i}{\partial r} + \mathrm{Re}\,\Phi^i\left(u\frac{\partial u}{\partial z}+v\frac{\partial u}{\partial r}\right)\right]$$
$$\times r^\alpha |J|\, d\xi\, d\eta - \frac{1}{\mathrm{Ca}}\int_0^{L_2}\frac{h^\alpha z_\xi}{\sqrt{z_\xi^2+h_\xi^2}}\frac{\partial \Phi^i}{\partial \xi}\bigg|_{\eta=1} d\xi$$
$$+\frac{1}{\mathrm{Ca}}\frac{h^\alpha z_\xi}{\sqrt{z_\xi^2+h_\xi^2}}\bigg|_{\eta=1,z=L_2} - \frac{\alpha}{\mathrm{Ca}}\int_0^{h_f}\frac{r}{h_f}\frac{\partial r}{\partial \eta}\Phi^i|_{\xi=1} d\eta,$$
$$i=1,2,\ldots,N, \tag{13}$$

$$R_v^i = -\int_{-L_1}^{L_2}\int_0^h \left[T^{zr}\frac{\partial \Phi^i}{\partial z} + T^{rr}\frac{\partial \Phi^i}{\partial r} + \mathrm{Re}\,\Phi^i\left(u\frac{\partial v}{\partial z}+v\frac{\partial v}{\partial r}\right)\right.$$
$$\left.+\alpha\frac{T^{\theta\theta}}{r}\Phi^i\right] r^\alpha |J|\, d\xi\, d\eta - \frac{1}{\mathrm{Ca}}\int_0^{L_2}\left[\alpha\Phi^i\sqrt{z_\xi^2+h_\xi^2}\right.$$
$$\left.+\frac{h^\alpha h_\xi}{\sqrt{z_\xi^2+h_\xi^2}}\frac{\partial \Phi^i}{\partial \xi}\bigg|_{\eta=1}\right] d\xi, \quad 1,2,\ldots,N, \tag{14}$$

$$R_K^i = \int_0^{L_2}(-uh_\xi + vz_\xi)\Phi^i|_{\eta=1} h^\alpha\, d\xi, \quad i=1,2,\ldots,S. \tag{15}$$

Here, M is the number of pressure unknowns, N the number of velocity unknowns, and S the number of free surface unknowns. Also, $|J|$ is the Jacobian of the isoparametric transformation, and α is a constant utilized to include the planar case in the final equations; for the planar jet r is substituted by y and $\alpha = 0$, whereas $\alpha = 1$ for the axisymmetric jet. The stresses in these equations at this point are substituted by $\mathbf{T} = -p\mathbf{I} + \tau$ where τ is given by Eq. (1).

The boundary terms of the momentum equations are substituted by the known normal and shear tractions at the free surface in terms of surface tension and curvature,[29]

$$\int_S \mathbf{n}\cdot\mathbf{T} = \int_S \frac{1}{\mathrm{Ca}}\frac{d\mathbf{t}}{dS}\phi^i dS = \frac{1}{Ca}[\mathbf{t}_1 - \mathbf{t}_2]\phi^i - \int_S \mathbf{t}\frac{d\phi^i}{dS}dS, \tag{16}$$

where **n** and **t** are the unit normal and tangent vectors to the free surface S, respectively. Along symmetry planes the shear traction is zero while elsewhere on the boundary the entire momentum equation is replaced by the essential conditions of known velocities.

The nonlinear system of Eqs. (12)–(15) can be written as

$$\mathbf{R}(\mathbf{x})=\mathbf{0}, \tag{17}$$

where $\mathbf{x}$ is the column vector of the nodal unknowns, and $\mathbf{R}$ is the column vector of the nonlinear weighted equations. This system is solved by Newton iteration

$$\mathbf{J}(\mathbf{x}^n)[\mathbf{x}^{n+1}-\mathbf{x}^n]=-\mathbf{R}(\mathbf{x}^n), \tag{18}$$

where $\mathbf{J}\equiv\partial\mathbf{R}/\partial\mathbf{x}$ is the Jacobian matrix. The set of linear equations is repeatedly solved by the frontal technique of Hood.[30] The tessellation is updated at each iteration by the newly found free-surface location values h_i, which are determined simultaneously with the primary unknowns u_i, v_i, and p_i.

In the transient formulation the time-dependent unknowns $\mathbf{u}(r,z,t)$, $p(r,z,t)$, and $h(z,t)$ are expanded in terms of biquadratic ϕ^i bilinear ψ^i, and quadratic $\phi^i|_{\eta=1}$, basis functions, respectively,

$$\mathbf{u}(r,z,t)=\sum_{1}^{N}\mathbf{u}_i(t)\phi^i(\xi,\eta), \tag{19}$$

$$p(r,z,t)=\sum_{1}^{M}p_i(t)\psi^i(\xi,\eta), \tag{20}$$

and

$$h(r,z,t)=\sum_{1}^{S}h_i(t)\phi^i(\xi,\eta)_{|\eta=1}, \tag{21}$$

where now the unknown nodal coefficients, $u_i(t)$, $p_i(t)$, and $h_i(t)$ are made time dependent. The time-dependent Galerkin residuals $\mathbf{R}$ are also obtained by weighting each of the governing equations with the basis functions themselves as in the steady case.

The spatial discretization reduces the time-dependent versions of Eqs. (12)–(15) to a system of ordinary differential equations,

$$\mathbf{M}\cdot\frac{\partial\mathbf{q}}{\partial t}+\mathbf{R}(\mathbf{q})=0, \tag{22}$$

where $q = [u_1(r,z,t),v_1(r,z,t),...,h_s(z,t)]$ is the vector of all the time-dependent nodal unknowns. The time derivatives are discretized by a standard backward-difference scheme,

$$\mathbf{M}\cdot\frac{\partial \mathbf{q}}{\partial t}=\mathbf{M}\cdot\left[\frac{\mathbf{q}^{n+1}-\mathbf{q}^{n}}{\Delta t}\right]=\mathbf{R}(\mathbf{q}^{n+1}). \tag{23}$$

Care must be taken when evaluating time derivatives on a moving tessellation, as it is the case here. The temporal derivatives are adjusted according to[31]

$$\frac{\partial \mathbf{u}}{\partial t}=\frac{d\mathbf{u}}{dt}-\left(\frac{dx}{dt}\frac{\partial \mathbf{u}}{\partial x}+\frac{dy}{dt}\frac{\partial \mathbf{u}}{\partial y}\right). \tag{24}$$

The left-hand side in Eq. (24) represents the actual local change of a variable with time. The first term on the right-hand side is the actual total change in a variable with time while the second term represents convective changes due to the moving tessellation. Equation (24) is substituted into Eq. (22) so that the term $\partial \mathbf{u}/\partial t$ is removed, allowing Eq. (23) to be solved at each time step by Newton iteration for the correct values of $\mathbf{u}$, p, and h. The initial conditions are those of a sinusoidally perturb jet from its steady state. This condition is imposed by perturbing the free surface of the initial basic flow. The corresponding perturbed initial velocity and pressure field is then determined from the steady-state governing equations after fixing the location of the free surface.

III. STEADY BINGHAM-PLASTIC JETS

A part of the mesh used for the finite axisymmetric jet is shown in Fig. 2. To check the accuracy of the finite-element predictions, we first compared the centerline and free-surface velocities, and the free surface elevation of the planar jet at $\mathrm{Re} = 0$ and $\mathrm{Ca} = 10^{-5}$ with the analytic solution to the stick-slip problem (plane creeping jet at infinite surface tension) by Richardson.[32] The predictions agree with the theory to within 0.1%. Significantly, these predictions were obtained as a limiting case, at $\mathrm{Re} = 0$ and $\mathrm{Ca} = 10^{-5}$, of the general solution, i.e., the location of the free surface was not fixed *a priori*. The expected planar interface in this limiting case was predicted to within 0.01%.

To analyze jets of Bingham plastic fluid, the tessellations for the Newtonian case were reused. The convergence was in general quadratic; however, at the continuation of the exponent m, convergence became slower as m increased. A zero-order continuation was used for all five

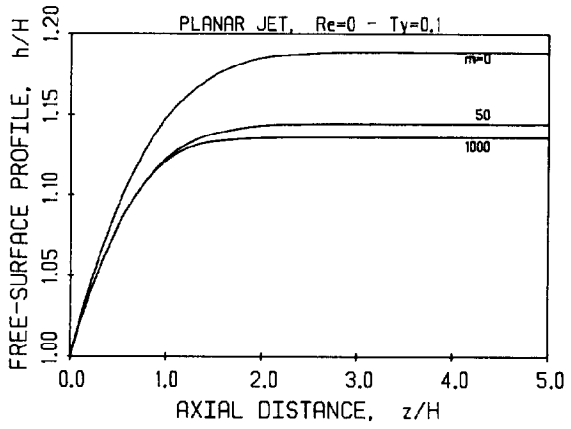

FIG. 3. Effect of exponent m on predicted free-surface profiles of a planar Bingham-plastic jet at $\mathrm{Re} = \rho UR/\mu = 0$ and $T_y = R\tau_y/\mu U = 0.1$. The predictions become independent of m for $m > 50$, which is taken to correspond to the ideal Bingham liquid.

parameters, in the order of Re, T_y, m, Ca, starting from lower Re, T_y, and m, and higher Ca. Continuation from one value of yield stress to a higher one failed to converge at high values of m. This pathology was cured by continuation with respect to m at constant yield stress, followed by continuation with respect to the yield stress at constant m as detailed in Papanastasiou.[13] Figure 3 shows the effect of the exponent m on the free-surface profiles of a plane jet; at relatively big values of m, where the ideal Bingham plastic is approached, the swelling becomes insensitive to the value of m. For our calculations, we demanded that the value of m was adequate to describe the ideal Bingham-plastic fluid, if the results deviated less than 0.01% from those at $m/10$. The value $m = 100$ proved to be sufficiently large to meet this criterion for all the ranges of the dimensionless parameters examined. Figure 3 indeed shows that Eq. (1) mimics the ideal Bingham plastic at large exponent $m > 100$.

No data for Bingham-plastic jets were found in the literature. However, a good test for the model and the finite element mesh would be the comparison of the predicted jet expansion at high Re with the theoretical limit at infinite Re. The asymptotic values of the expansion of round and planar jets at infinite Re as functions of T_y are derived by assuming that the velocity profile at the exit of the die is given by Eqs. (3) and

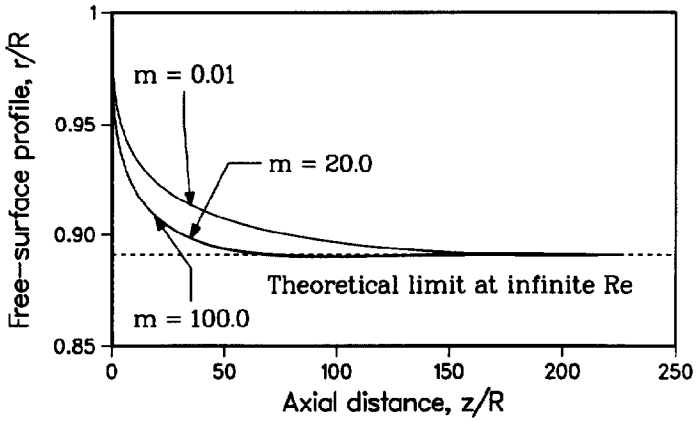

FIG. 4. Predicted free surface profiles for a round Bingham plastic jet at $\mathrm{Re} = \rho UR/\mu = 2000$, $\mathrm{Ca} = \mu U/\sigma = 10^6$, and dimensionless $T_y = R\tau_y/\mu U = 2$.

(4), respectively, and is flat at a plane very far downstream. Mass and momentum balances between the two locations show that the theoretical final half thickness is

$$h_{f\infty} = \frac{60C^3}{(8C + 7T_y)(C - T_y)^4} \tag{25}$$

for the planar jet, and the final radius is

$$h_{f\infty} = \left[\frac{60}{5C^2 + 6T_yC + 4T_y^2}\right]^{1/2} \frac{C^2}{(C - T_y)^2} \tag{26}$$

for the round jet. C is the constant pressure gradient given by Eqs. (6) and (7). The above expressions give the Newtonian limits, 0.83333 and 0.8660 for cylindrical and planar jets, respectively, for zero yield stress T_y, and they both go to 1 as $T_y \to \infty$. The finite-element predictions at $\mathrm{Re} = 2000$ agree with the theoretical results of Eqs. (25) and (26). As it is shown in Fig. 4 , the predicted expansions approach their theoretical limit very far downstream, independent of the value of m.

The effect of the yield stress T_y on the calculated profiles at $\mathrm{Re} = 0$ and 15 is illustrated in Figs. 5 and 6, respectively. As the yield stress increases, the swelling at low Re and the contraction at higher Re are reduced. These results are due to the increased tendency for the center core of the jet to exit the die as a solid plug when T_y is increased. The

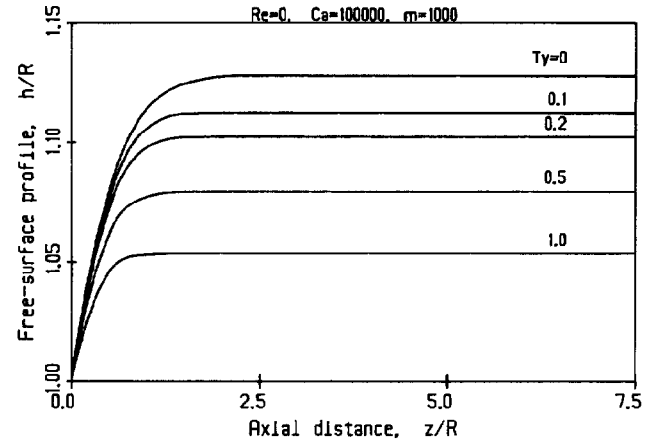

FIG. 5. Effect of dimensionless yield stress, $T_y = R\tau_y/\mu U$, on free-surface profiles of a round Bingham-plastic jet at $\mathrm{Re} = \rho UR/\mu = 0$, $\mathrm{Ca} = \mu U/\sigma = 10^6$, and $m = 1000$.

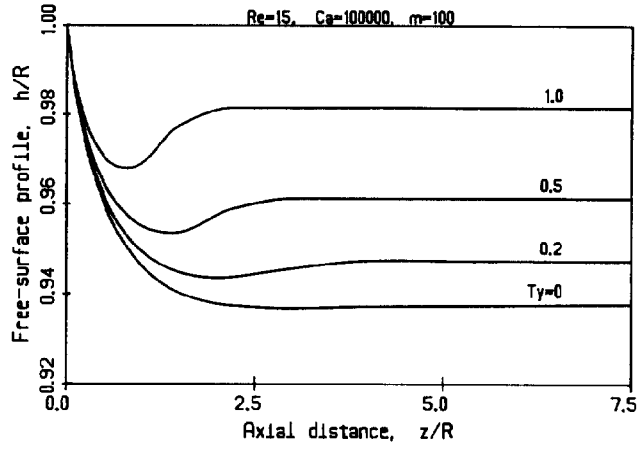

FIG. 6. Effect of dimensionless yield stress, $T_y = R\tau_y/\mu U$, on free-surface profiles of a round Bingham-plastic jet at $\mathrm{Re} = \rho UR/\mu = 15$, $m = 100$, and $\mathrm{Ca} = \mu U/\sigma = 10^6$.

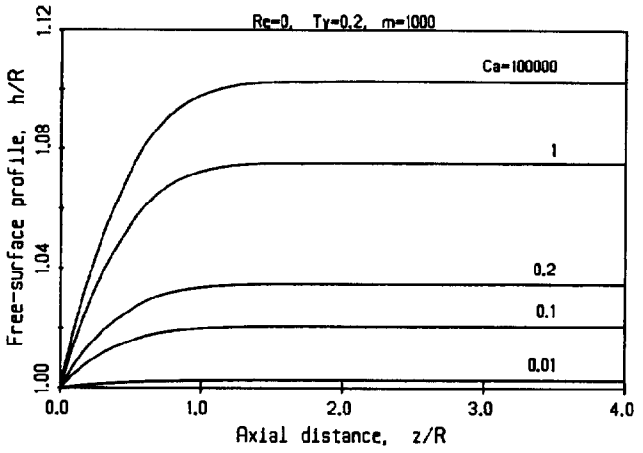

FIG. 7. Effect of dimensionless surface tension, $Ca = \mu U/\sigma$, on free-surface profiles of a round Bingham-plastic jet at $Re = \rho UR/\mu = 0$, $m = 1000$, and $T_y = R\tau_y/\mu U = 0.2$.

effect of yield stress is analogous to that of surface tension. Necking of the jet occurs as T_y increases for higher Re. Nevertheless, for even higher values of T_y the necking vanishes. This can be attributed to the fact that the free surface of the yielded liquid under negligible surface tension tends to follow the interior line dividing the yielded and the solid-like unyielded region. As the material exits the die, there is a depression of the unyielded core[13] (and therefore extension of the yielded region to the interior) due to the large velocity gradient near the exit singularity, which serves to produce the neck for finite values of T_y. Predictions at various capillary numbers, $Re = 0$, and $T_y = 0.2$ are shown in Fig. 7 . As it is expected, surface tension reduces swelling. At low surface tension the swelling is reduced more than that of the Newtonian liquid, due to the superimposed yield-stress effect. However, the profiles at $Ca \leqslant 0.5$ are close to those of the Newtonian jet and therefore the effect of yield stress weakens at high surface tension.

IV. TRANSIENT ANALYSIS

The results presented here are for infinite circular and planar jets. The jet is assumed to be in a steady state of plug flow at $t < 0$ and at $t = 0$ a sinusoidal perturbation of 5% of the diameter or thickness is imposed according to the expression

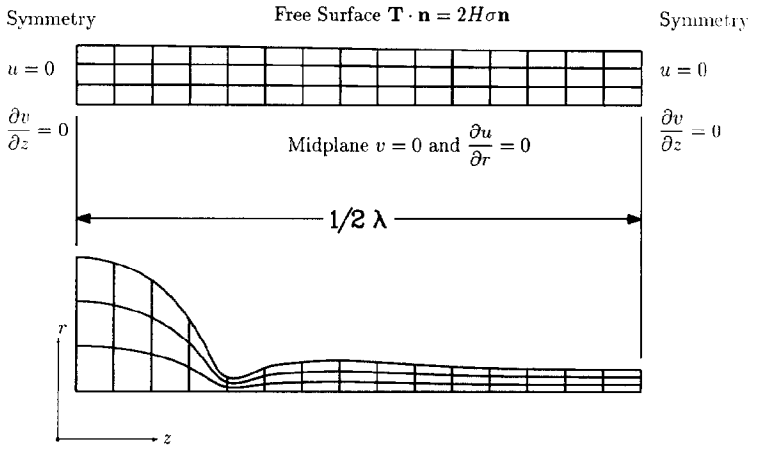

FIG. 8. The appropriate periodic boundary conditions for the infinite jet, with a typical tessellation. Each element shown is a biquadratic Lagrangian element.

$$h = 1.0 + 0.05 * \sin(\pi z/\lambda), \tag{27}$$

where λ is the wavelength of the disturbance. Strictly speaking, such a study should be performed at the most unstable (fastest growing) wavelength. Unfortunately, a nonlinear analysis of the most unstable wavelength for each of the many parameter settings is not practical given the fact that this wavelength function of all of the dimensionless groups. For this reason, the dimensionless wavelength was fixed to a value of $\lambda = 20$ which lies between the theoretical values[23] of $\lambda = 9.8$ an inviscid jet and $\lambda \to \infty$ for a jet dominated by purely viscous stresses. The progression of the finite disturbance is monitored at times $t > 0$ by solving the time-dependent conservation equations for the velocities, pressures, and free surface locations jet radius of thickness. Since it is assumed that there is no interaction with the surrounding air, the coordinate system was translated with the steady plug flow velocity. This allows the jet to be viewed as a stationary liquid cylinder at $t = 0$. Consequently, there is no physical reference velocity in the problem and all velocities are scaled with the quantity σ/μ, where μ is the viscosity of the liquid and σ is the surface tension. The governing equations are those given earlier with the following replacements:

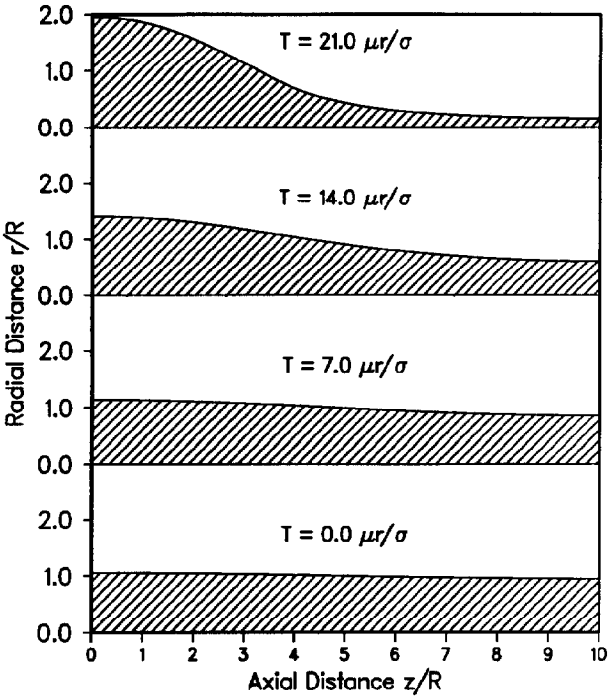

FIG. 9. The collapsing flow domain of a jet with dominating viscous forces, i.e., for $\rho\sigma R/\mu^2 \to 0$, at several time intervals T, which is made dimensionless by the quantity $\mu r/\sigma$.

$$\mathrm{Re} \to J = \frac{\rho\sigma R}{\mu^2} = \frac{1}{Z^2},$$

$$\mathrm{Ca} \to 1,$$

where Z is the Ohnesorge number. J has the physical significance of being the ratio (surface tension force) (inertial force)/(viscous force).[2] All other dimensionless groups can be modified by taking $U = \sigma/\mu$. The domain and the boundary conditions are illustrated in Fig. 8 along with a typical tesselation; due to the assumed infinite length, there is symmetry at the beginning and the end of a half-wavelength so that the problem can be examined on a finite domain, accordingly.

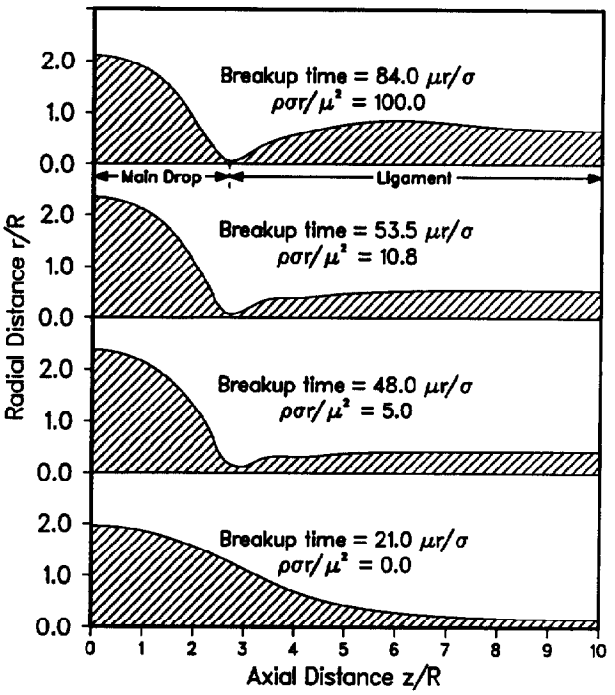

FIG. 10. The final jet flow domain is shown for various values of $J = \rho\sigma R/\mu^2$ for a Newtonian filament.

In addition to a common power-law (shear-thinning) viscosity which is widely used in steady flow calculations, a second strain-rate viscosity was examined in Eqs. (13) and (14) by using the more realistic Carreau model,[33]

$$\frac{\mu-\mu_\infty}{\mu_0-\mu_\infty}=[1+(\lambda^*\Pi_D)^2]^{(n-1)/2}, \tag{28}$$

where n is the power law exponent that yields shear thinning and Newtonian liquids for $n<1$ and $n=1$, respectively. The constants μ_0 and μ_∞ are the zero-shear and infinite-shear viscosities while λ^* is a characteristic relaxation time. The Carreau model was used to cure the pathology of the power-law model, which at vanishingly small strain rates predicts an infinitely large viscosity and is, therefore, inappropriate

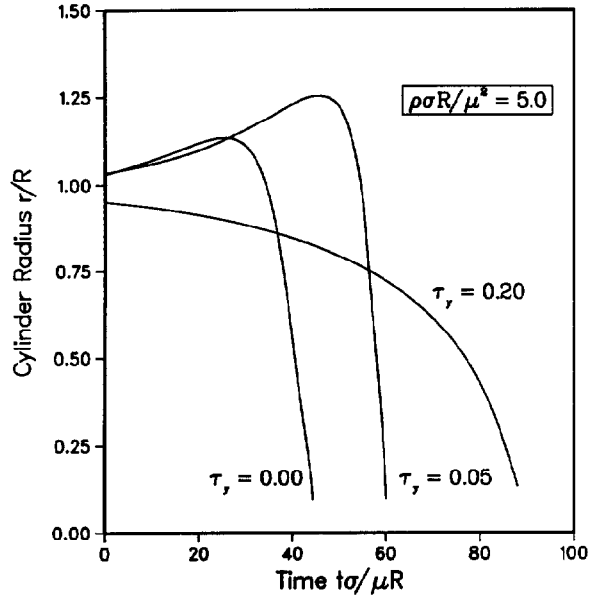

FIG. 11. The neck radius evolution near the jet break point is shown as a function of time for $J = \rho\sigma R/\mu^2 = 5$ and several values of dimensionless yield stress, $T_y = \tau_y/R\sigma$.

in regions where the disturbance becomes vanishingly small. Indeed, as it will be demonstrated below, this pathology may lead to incorrect stability results.

Typical stability results are shown in Fig. 9 for an infinite Newtonian cylinder with dominating viscous forces ($J = 0$). The dimensionless time increment Δt, used for this and all subsequent computations was 0.05. This value for Δt was arrived at by demanding that successive runs with decreasing Δt produce similar results. It is obvious that in the case of $J = 0$ the plug-flow infinite cylinder is unstable because the amplitude of its disturbance grows with time and reaches half-diameter after 29 time units. The initial growth rate was found to agree well with that obtained by linear theory[23] as shown in Fig. 13. The cylinder is about to break forming a single droplet per wavelength of the disturbance.

Figure 10 illustrates the final jet dimensions (close to the final breakage) for various values of J. The results shown for $J = 10.8$ correspond

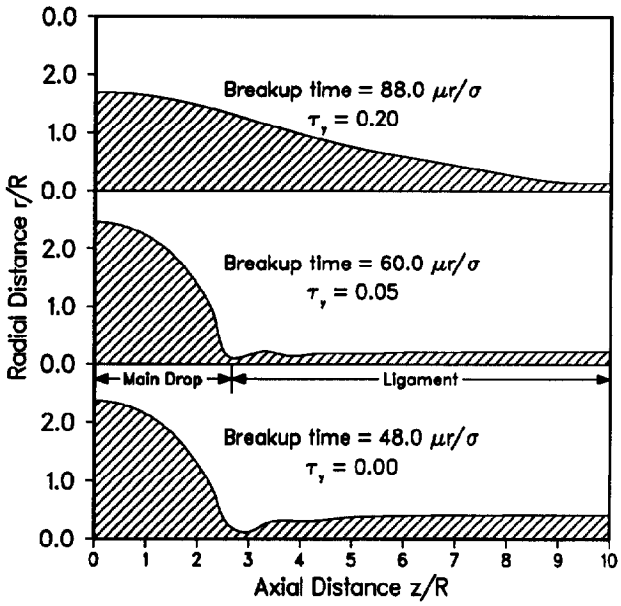

FIG. 12. The final jet flow domain is shown for various values of dimensionless yield stress, $T_y = \tau_y/R\sigma$, with $J = \rho\sigma R/\mu^2 = 5$.

to a glycerine and water solution and agree with results reported elsewhere.[25,26] The tendency to form a droplet which has a minimum surface energy to volume ratio is clearly seen. It is also evident from this figure that a ligament is formed between successive main drops which is well documented experimentally.[27,34–36] This ligament would, at later times, form another droplet referred to as a satellite drop which is generally considered to be detrimental to processes involving atomization.[37] As J increases, larger and larger ligaments are formed leading to larger satellite droplets.

The same numerical experiments, with surface tension, were repeated for Bingham liquids and for liquids with shear-rate dependent viscosity. The results are summarized in Figs. 11 through 14. It should be noted that these calculations were made possible because of the convenient constitutive equation that does not require tracking of yield surfaces, in time or in space.

From an intuitive standpoint, the introduction of yield stress (here measured in units of σ/R) should delay the breakup process or, in other

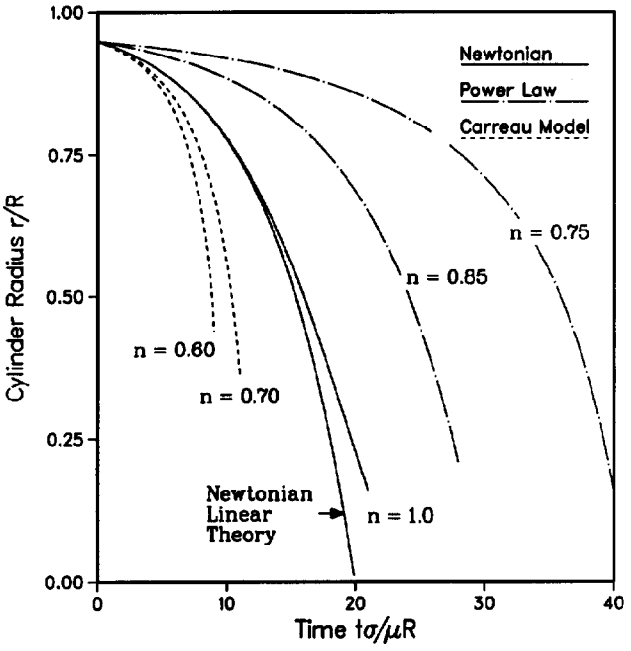

FIG. 13. The neck radius evolution near the jet break point is shown as a function of time for a Carreau fluid ($\mu_\infty/\mu_0 = 0.1$) and a power-law fluid with $J = \rho\sigma R/\mu^2 = 0$. Also shown is the prediction of linear theory for a Newtonian fluid (Ref. 23).

words, move the jet closer to neutral stability. This behavior is illustrated in Fig. 11 in which the progression of the disturbance at the final jet breaking point is plotted as a function of time for different values of the dimensionless yield stress $T_y = \tau_y R/\sigma$. As the yield stress increases, the collapse of the jet is delayed and the final breakup time is prolonged. Figure 12 shows the effect of yield stress on the volume of the satellite droplet. An increased yield stress first produces very thin ligaments, then no ligaments at all. Thus, the introduction of yield stress produces smaller satellite drops and causes a delay of jet breakup, given a fixed disturbance wavelength. High yield stress however results in droplets of uniform size, without any satellite drops, which is of interest to ink-jet and paint atomization.[27,37]

Calculations were also performed for fluids exhibiting shear thinning but no yield stress. Both the power-law and the Carreau model were

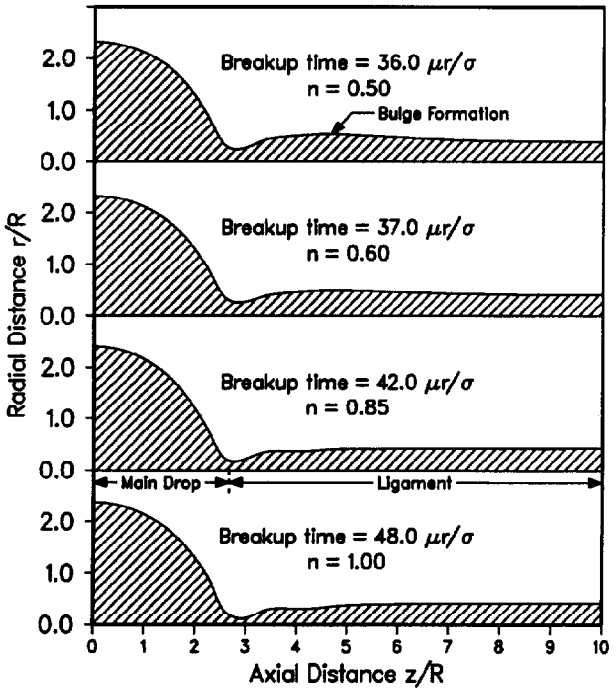

FIG. 14. The final jet flow domain is shown for various values of the Carreau shear-thinning parameter n with $J = \rho\sigma R/\mu^2 = 5$ and $\mu_\infty/\mu_0 = 0.1$.

examined. Figure 13 shows results for such fluids with negligible inertial terms. The power-law model predicts that increased shear thinning (decreasing exponent n) will delay the breakup time while the Carreau model (for decreasing n) shows the opposite. This anomaly is due to the fact that the power-law model is singular as $\dot{\gamma} \to 0$, resulting in a huge viscosity for small $\dot{\gamma}$. This artificially induced viscosity is initially large enough to predict a significant artificial delay of the breakup of the jet. The Carreau model, with a finite zero-shear viscosity, avoids this artificiality. In fact, it is well known that viscosity dissipates energy and is therefore a stabilizing factor; thus, shear thinning, which reduces viscosity, is expected to destabilize the jet leading to shorter breakup times. Figure 14 illustrates the effect of shear thinning on satellite drop size. At the neck of the jet, the shear rates are relatively high, which reduces the viscosity, which in turn reduces resistance to collapse. Thus, once a neck

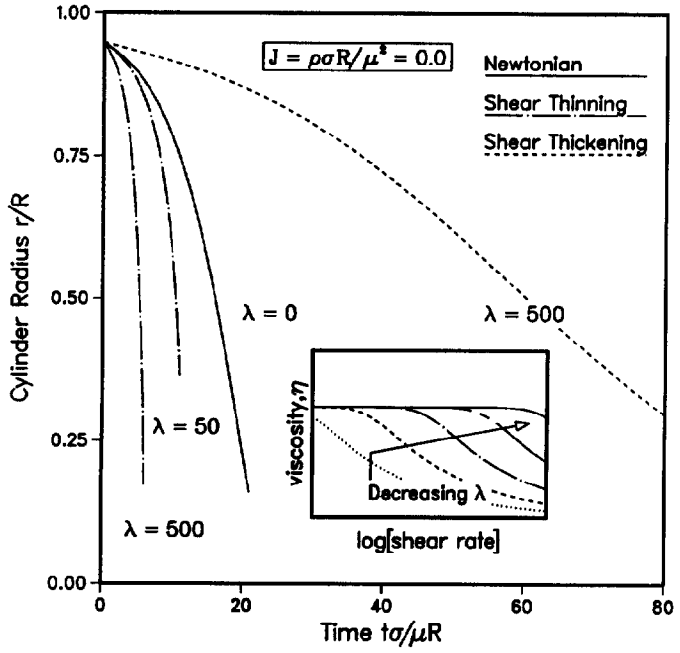

FIG. 15. The neck radius evolution near the jet break point is shown as a function of time for a Carreau fluid with various values of the relaxation constant λ with $J = \rho\sigma R/\mu^2 = 0$, $n = 0.7$, and $\mu_\infty/\mu_0 = 0.1$.

is formed, the jet collapses very quickly trapping a larger volume of the fluid in the ligament, which results in larger satellite droplets.

The Carreau model allows the onset of shear thinning to be delayed by decreasing its time constant λ^*. This effect is shown in Fig. 15 , in which increasing λ^* has a qualitatively similar effect as decreasing n; that is, it produces shorter breakup times. As explained above, quicker breakup times indicate that the ligament (or satellite) volume would increase. This fact is again shown in Fig. 16 where the final jet configuration is plotted for various values of λ^*.

As expected, the corresponding calculations for planar sheets showed that surface tension enhances stability. Yield stress did not produce unstable sheets; the only effect yield stress had was to delay the leveling of the initial sinusoidal disturbance. Shear-thinning sheets behaved

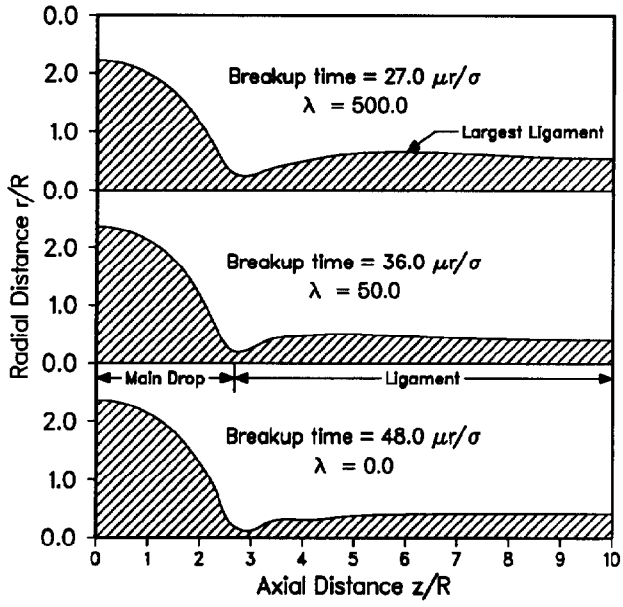

FIG. 16. The final jet flow domain is shown for various values of the Carreau time constant λ with $J = \rho\sigma R/\mu^2 = 5$, $n = 0.7$, and $\mu_\infty/\mu_0 = 0.1$.

much like stable Newtonian sheets since low shear rates resulted in nearly constant viscosity.

V. CONCLUSIONS

The combination of Galerkin finite element and a convenient Bingham-plastic model, which is valid uniformly in yielded and unyielded regions, produced an efficient scheme for computation of flows of materials with yield. The efficiency and attractiveness of the scheme is due to the fact that it eliminates tracking the location of yield surfaces, which makes possible the implementation of global Newton iteration to solve the resulting nonlinear equations. Thus, in this way, there is really little or no difference between algorithms for Newtonian and Bingham plastic liquids; the only difference being the stress law inserted in the momentum equation.

For the steady jet calculations, the asymptotic behavior of this scheme was similar to that exhibited by the ideal Bingham model; the

predictions at Re = 2000 agreed with the asymptotic values of the swelling of the ideal Bingham-plastic liquid at infinite Re, for both circular and planar jets. Yield stress was found to suppress the swelling or the contraction of the jet and to induce necking at moderate Reynolds numbers. The effect of yield stress is similar to and often masked by high surface tension coexistence.

Stability results have shown that increased surface tension will result in larger ligament volumes (ultimately leading to larger satellite droplets) due to the quick snapoff at the neck where curvature is high. Yield stress increases the breaking time of the jet and reduces the size of the resulting satellite. The latter is attributed to the delay in the breaking time which allows the fluid in the ligament longer time to overcome its own inertia and pass into the main droplet. The opposite effect was observed with increasing shear thinning, which resulted in larger satellite droplets.

ACKNOWLEDGMENTS

This research is being sponsored by grants-in-aid from General Motors Corporation, whose support is gratefully acknowledged. All computational results were obtained on the IBM 3090-600E/VM at the University of Michigan.

NOTATION

Ca	= Capillary number ($\mu U/\sigma$)
$\mathbf{D}$	= rate of strain tensor
h	= elevation of free surface
h_f	= final jet dimension
$2H$	= mean curvature of free surface
J	= redefined transient Reynolds number($\rho\sigma R/\mu^2$)
$\lvert J\rvert$	= Jacobian of the isoparametric transformation
$\mathbf{J}$	= Jacobian of the residuals $\mathbf{R}$ with respect to unknowns $\mathbf{x}$
L_1, L_2	= distances of inlet and outlet from exit
M, N, S	= numbers of pressure, velocity, and free-surface elevation unknowns
n	= exponent in power-law model
$\mathbf{n}$	= unit normal vector
m	= exponent in Bingham-plastic model
p	= dimensionless pressure
R	= radius
$\mathbf{R}$	= vector of residuals

R_C^i, R_K^i, $\mathbf{R}_M^i$ = continuity, kinematic, and momentum residuals
R_u^i, R_v^i = z- and r-momentum residuals
Re = Reynolds number (pUR/μ)
$\mathbf{t}$ = unit tangent vector
$\mathbf{T}$ = dimensionless stress tensor
T^{rr}–, T^{rz}–, T^{zz}–, $T^{\theta\theta}$– = rr, rz, zz, and $\theta\theta$ components of stress tensor
T_y = dimensionless yield stress ($\tau R/\mu U$)
u = axial velocity component
$\mathbf{u}$ = dimensionless velocity
U = mean velocity
v = radial velocity component
$\mathbf{x}$ = vector of nodal unknowns
Z = the Ohnesorge number

Greek letters

α = parameter in Eqs. (12), (13), (14), and (15)
μ = viscosity
μ_0 = zero-shear viscosity
μ_∞ = infinite-shear viscosity
λ = wavelength of disturbance
λ^* = time constant in Carreau model
ξ, η = isoparametric coordinates
ρ = density
σ = surface tension
τ_y = yield stress
Φ^i, Ψ^i = biquadratic and bilinear basis functions

References

1. E. C. Bingham, *Fluidity and Plasticity* (McGraw–Hill, New York, 1922), p. 215.
2. J. G. Oldroyd, "A rational formulation of the equations of plastic flow for a Bingham solid," Proc. Cambridge Philos. Soc. **43**, 100, 383 (1947).
3. M. Reiner, "Ten Lecture on Theoretical Rheology," Th. Rheol. **49**, 133 (1943).
4. W. Prager, *Introduction to Mechanics of Continua* (Ginn, Boston, 1961).
5. R. B. Bird, G. C. Doi, and B. J. Yarusso, "The rheology of flows of viscoplastic materials," Rev. Chem. Eng. **1**, 1 (1982).
6. A. B. Metzner, "Rheology of suspensions in polymeric liquids," J. Rheol. **29**, 739 (1985).
7. A. G. Fredrickson, *Principles and Applications of Rheology* (Prentice Hall, Englewood Cliffs, NJ, 1964).
8. A. S. Argon, *Constitutive Equations in Plasticity* (MIT, Cambridge, MA, 1975).
9. L. E. Malvern, *An Introduction to the Mechanics of the Continuous Medium* (Prentice Hall, Englewood, NJ, 1969).

10. H. A. Barnes and K. Walter, "The yield stress myth," Rheol. Acta **24**, 323 (1985).
11. J. P. Harnett and R. Y. Z. Hu, J. Rheol. **33**, 671 (1989).
12. G. Astarita, J. Rheol. **34**, 275 (1990).
13. T. C. Papanastasiou, "Flows of materials with yield," J. Rheol. **31**, 385 (1987).
14. M. Keentok, J. F. Milthorpe, and E. O'Donovan, "On the shearing zone around rotating vanes in plastic liquids: theory and experiment," J. Non-Newt. Fluid Mech. **17**, 23 (1985).
15. N. Q. Dzuy, and D. V. Boger, "Direct yield stress measurement with the vane method," J. Rheol. **29**, 334 (1985).
16. J. L. White, Y. Wang, A. I. Isayev, N. Nakajima, F. C. Weissert, and K. Min, "Modeling of shear viscosity behavior and extrusion through dies for rubber compounds," Rubber Chem. Technol. **60**, 337 (1986).
17. A. N. Beris, J. A. Tsamopoulos, R. C. Armstrong, and R. A. Brown, "Creeping motion of a sphere through a Bingham plastic," J. Fluid Mech. **158**, 219 (1985).
18. D. K. Gartling and N. Phan-Thien, "A numerical simulation of a plastic fluid in a parallel-plate plastometer," J. Non-Newt. Fluid Mech. **14**, 347 (1984).
19. G. G. Lipscomb and M. M. Denn, "Flow of Bingham fluids in complex geometries," J. Non-Newt. Fluid Mech. **14**, 337 (1984).
20. C. R. Beverly, and R. I. Tanner, "Numerical Analysis of extrudate swell in viscoelastic materials with yield stress," J. Rheol. **33**, 6 (1989).
21. M. Bercovier and M. Engelman, "A finite element method for incompressible non-Newtonian flows," J. Comp. Phys. **36**, 313 (1980).
22. L. Rayleigh, "On the instability of jets," London Math. Soc. **10**, 4 (1879).
23. S. Chandrasekhar, *Hydrodynamic and Hydromagnetic Stability* (Clarendon, Oxford, 1961).
24. M. R. Goldin, R. Pfeffer, and R. Shinnar, "Break-up of a capillary jet of a Non-Newtonian fluid having a yield stress," Chem. Eng. J. **4**, 8 (1972).
25. R. Keunings, "A finite element method for a class of viscoelastic flows in deforming domains applied to jet break-up," Proceedings IX International Congress of Rheology, Mexico, 1984, p. 699.
26. D. W. Bousfield, R. Keunings, G. Marrucci, and M. M. Denn, "Nonlinear analysis of the surface tension driven breakup of viscoelastic filaments," J. Non-Newt. Fluid Mech. **21**, 79 (1986).
27. M. Goldin, R. Pfeffer, and R. Shinnar, "Break-up of a Capillary Jet of a Non-Newtonian Fluid having a Yield Stress," Chem. Eng. J. **4**, 8 (1972).
28. W. J. Silliman and L. E. Scriven, "Separating flow near a static contact line: Slip at a wall and shape of a free surface," J. Comp. Phys. **34**, 287 (1980).
29. K. J. Ruschak, "A three-dimensional linear stability analysis for two-dimensional free boundary flows by the finite element method," Comput. Fluids **11**, 391 (1983).
30. P. Hood, "Frontal solution program for unsymmetric matrices," Int. J. Numer. Meth. Eng. **10**, 379 (1976).
31. H. S. Kheshgi, and L. E. Scriven, "Penalty-finite element analysis of unsteady free surface flows," in *Finite Elements in Fluids, Vol. 5*, edited by J. T. Oden *et al.* (Wiley, New York, 1983).
32. S. Richardson, "A stick-slip problem related to the motion of a free jet at low Reynolds numbers," Proc. Cambridge Philos. Soc. **67**, 477 (1970).
33. R. B. Bird, R. C. Armstrong, and O. Hassager, *Dynamics of Polymeric Liquids*, (Wiley, New York, 1977), p. 218.
34. E. F. Goedde and M. C. Yuen, "Experiments on liquid jet instability," J. Fluid Mech. **40**, 495 (1970).

35. D. F. Rutland, and G. J. Jameson, "Theoretical prediction of the sizes of drops formed in the breakup of capillary jets," Chem. Eng. Sci. **25,** 1689 (1970).
36. W. T. Pimbley and H. C. Lee, "Satellite droplet formation in a liquid jet," IBM J. Res. Dev. **21,** 21 (1977).
37. D. B. Bogy, "Drop formation in a circular liquid jet," Annu. Rev. Fluid Mech. **11,** 207 (1979).